Pergamon

Chaos, Solitons & Fractals Vol. 5, No. 10, pp. 2023–2045, 1995
Copyright © 1995 Elsevier Science Ltd
Printed in Great Britain. All rights reserved
0960–0779/95$9.50 + .00

0960–0779(94)00177-4

Flux Tubes and Scaling in MHD Dynamo Simulations

AXEL BRANDENBURG

HAO/NCAR, P.O. Box 3000, Boulder, CO 80307, USA

Abstract—MHD simulations of compressible convection in a layer heated from below are discussed and the results analysed in various ways. The ultimate aim of these simulations is to understand the generation and evolution of the magnetic field in the sun. The formation of flux tubes is addressed, and it is concluded that random field line stretching plays the dominant role, which is in contrast to vortex tubes where both shear instabilities and vortex stretching contribute almost equally to the generation of vorticity. Magnetic flux tubes occur preferentially near stagnation points, but there remains a significant flow component along the tube. Various scaling properties of the magnetic field generated in such simulations are investigated. Multifractal dimensions, cancellation exponents, and generalized power spectra are computed. While the spectra show a tendency for power law scaling, no such behavior is found for the cancellation exponent. Finally, implications for the generation of large-scale fields in the solar dynamo are discussed.

1. INTRODUCTION

In astrophysics many examples of spontaneous formation of structures are known. Nonlinear hydrodynamic effects are often the cause of such phenomena of self-organization. The spontaneous generation of magnetic fields by a dynamo process can give rise to the formation of large-scale magnetic fields that lead to a systematic orientation of sunspot pairs and to their variation with an eleven-year period. This process has often been described in terms of mean-field dynamo theory [1]. Meanwhile, three-dimensional simulations of the full MHD equations have been carried out that show the spontaneous formation of magnetic fields from a weak seed magnetic field [2–8].

Some kind of dynamo mechanism is also believed to operate in stars, planets, galaxies and accretion disks. Although the physical processes are different in the various cases, they all have in common that the magnetic energy results from fluid motions. Those motions are expected to be turbulent, because the Reynolds number is very large. Estimates for the solar convection zone lead to $\mathrm{Re} = \mathcal{O}(10^{16})$ [9], and consequently a wide range of spatial and temporal scales is involved in the problem. Direct simulations with realistic values for the viscosity are therefore impossible, although we hope that some essential physics can already be captured in simulations with much lower Reynolds number.

Above a certain critical magnetic Reynolds number, $R_m = u_t L/\eta$, there is spontaneous dynamo action: the magnetic field begins to grow exponentially on a dynamical time scale, $\tau = L/u_t$, until saturation sets in (see Fig. 1 in ref. [8]). Here, L is an outer length scale (comparable to the density scale height of the fluid), u_t the turbulent rms-velocity, and η the magnetic diffusivity. For the sun we expect $R_m = \mathcal{O}(10^8)$ [9]. This is well above the threshold for dynamo action, which is of the order of one hundred. The generated magnetic field appears as coherent flux tubes, similar to the vorticity which is also concentrated into tubes [10–12]. In the simulations presented in refs [8, 13], as much as 25% of the magnetic field is inside flux tubes, whose strengths exceed a quarter of the

maximum field strength, but which occupy only 5% of the volume [13]. In other words, the magnetic field is spatially intermittent.

Most of the magnetic flux is generated in the surroundings of strong convective downdrafts that tend to push the flux tubes downwards to the bottom of the convection zone. This has been shown using a selective analysis of the work done against the Lorentz force for regions with upward and downward velocities. Thus, while dynamo action occurs throughout the convection zone, there is a strong tendency for the magnetic field to accumulate in the interface between the convection zone and the radiative interior. It is believed that in the sun flux tubes emerge from such an interface which then produce bipolar regions and sunspot pairs when they reach the surface. In the dynamo simulations, however, only a small portion of the magnetic field comes to the surface. In spite of the effect of magnetic buoyancy, the turbulent 'pumping' mechanism mentioned above is able to keep the field down long enough to be regenerated by dynamo action [8].

A statistical analysis of the hydromagnetic flow reveals useful information about the correlations between velocity, vorticity and magnetic field vectors. The probability density functions of the angles between vectors of the magnetic field, velocity, and vorticity show a tendency for the magnetic field vectors to be aligned with the vorticity mainly in the lower overshoot layer, but aligned with the velocity in the bulk of the convection zone. Details of this analysis can be found in ref. [13]. In the following section we investigate properties of flux tubes and begin with the question of how such flux tubes are generated.

The analysis presented in this paper is based on a particular snapshot of a simulation with Rayleigh number $\mathrm{Ra} = 10^6$, Prandtl number $\mathrm{Pr} \equiv \nu/\bar{\chi} = 0.2$, and magnetic Prandtl number $\mathrm{Pr}_M \equiv \nu/\eta = 4$ [8, 13], where ν is the kinematic viscosity and $\bar{\chi}$ the average thermal conductivity. For identification with previous investigations using the same data [8, 13, 14], we mention that the time of this snapshot is $t = 779$ time units since the beginning of the simulation. The unit of time is $[t] = (d/g)^{1/2}$ (related to free-fall times), where d is the thickness of the unstable layer and g is gravity. One turnover time is about 15 time units. The resolution is 63^3 mesh points and the widths of the domain in the x- and y-directions are both $2d$. We begin by investigating the formation and shape of flux tubes (Section 2), turn then to different descriptions of the scale dependence of the magnetic field (Section 4), and discuss finally some implications for solar dynamos (Section 5).

2. FLUX TUBES

2.1. *Alignment*

In order to investigate the properties and generation of magnetic flux tubes in more detail, it is useful to investigate the correlations of the magnetic field with the eigenvectors of the rate of strain matrix, $s_{ij} = \frac{1}{2}(u_{i,j} + u_{j,i})$. In simulations of hydrodynamical turbulence [12, 15, 16] corresponding investigations have revealed an enhanced alignment of the vorticity, $\boldsymbol{\omega}$, and the intermediate eigenvector $\mathbf{e}_2$ of the strain matrix. This is the eigenvector corresponding to the intermediate eigenvalue λ_2 which, on average, turns out to be positive. Furthermore, the vorticity tends to be perpendicular to the directions of compression *and* stretching, corresponding to the directions of the eigenvectors $\mathbf{e}_1$ and $\mathbf{e}_3$ with the smallest (most negative) and largest eigenvalues λ_1 and λ_3, respectively.

Vortex tubes are believed to be generated by an instability associated with shearing motions [17]. Such a shearing motion can be decomposed into rotational and straining motions, where the eigenvectors $\mathbf{e}_1$ and $\mathbf{e}_3$ determine the major axes of the straining motion; see Fig. 1. The vortex tubes must then be locally perpendicular to the straining motion, i.e. $\boldsymbol{\omega}$ has to be perpendicular to both $\mathbf{e}_1$ and $\mathbf{e}_3$ and, since the three eigenvectors

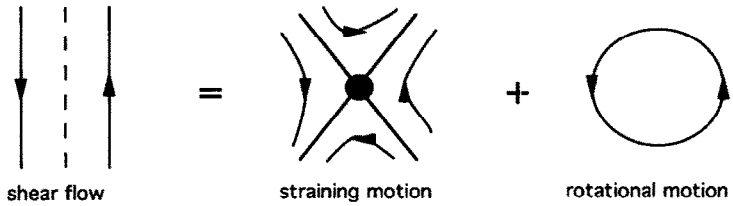

Fig. 1. Sketch illustrating the formation of a tube from a shear flow. The shear flow is decomposed into straining and rotational motions.

are orthogonal, ω must be aligned with $\mathbf{e}_2$ [18–20]. Because of the similarity between vortex tubes and magnetic flux tubes, it is tempting to apply the same ideas to the generation of magnetic flux tubes as well.

In the present case of compressible flows, the relation $\lambda_2 = -(\lambda_1 + \lambda_3)$, which is true for incompressible flows, is only approximately satisfied. In incompressible flows the various alignment properties apply especially to those points where $\lambda_2 > 0$. However, the more fundamental criterion is $\lambda_1 + \lambda_3 < 0$, and it is this one which remains relevant even in the compressible case. In Fig. 2 we present the probability functions for the cosines of the angles between the three eigenvectors and ω and the magnetic field $\mathbf{B}$.

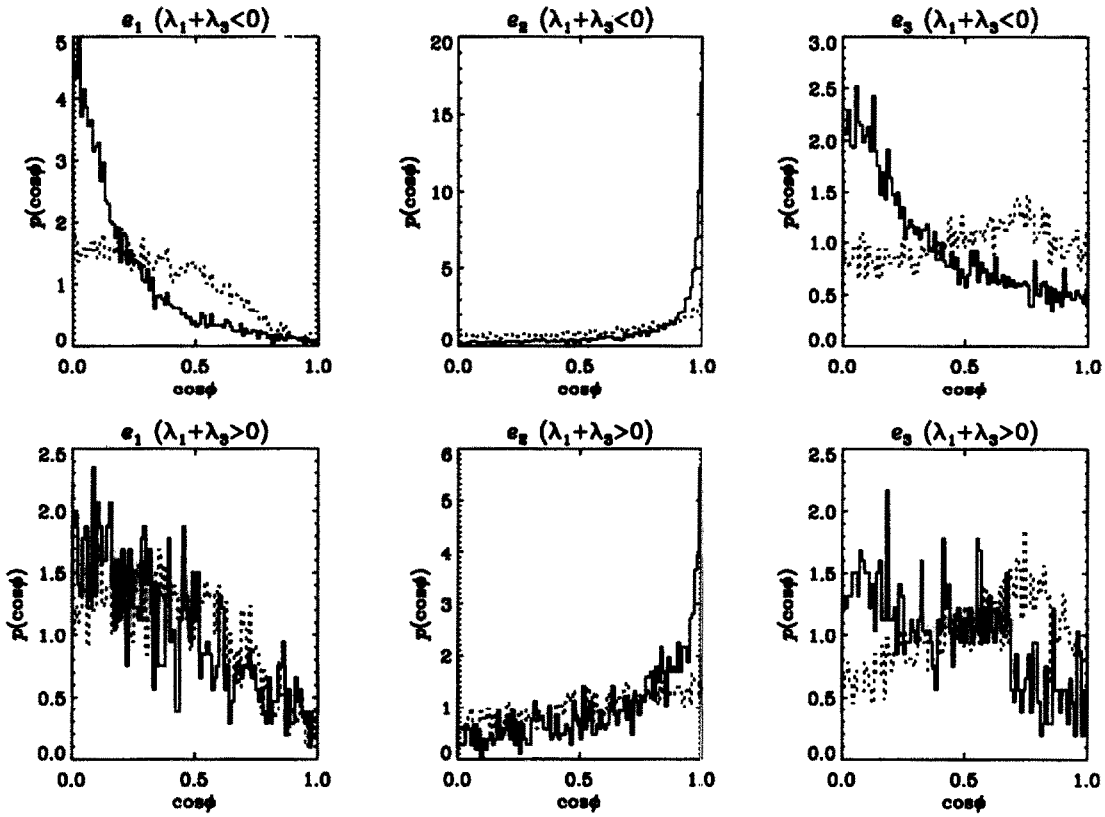

Fig. 2. Selective analysis of the correlations between the three eigenvectors of the rate of strain tensor and vorticity (solid lines) and magnetic field (dotted line). Only those points where $|\omega| > 2 = 0.27\omega_{\max} \approx 2.7\omega_{\rm rms}$ (solid lines for correlation with ω) and $|\mathbf{B}| > 0.04 = 0.28B_{\max} \approx 2.2B_{\rm rms}$ (dotted lines for correlation with $\mathbf{B}$) are considered here. The upper row is for those points where $\lambda_1 + \lambda_3 < 0$, and the lower one for $\lambda_1 + \lambda_3 > 0$.

The most pronounced alignment is clearly between $\boldsymbol{\omega}$ and $\mathbf{e}_2$. This is especially the case in the dynamo run where the probability density $p(\cos\phi)$ attains values around 17; see Fig. 2. (As usual, p is normalized such that $\int p \, \mathrm{d}\cos\phi = 1$.)

Some of the alignment properties of $\boldsymbol{\omega}$ apply also to $\mathbf{B}$, but the trends are less clear than for $\boldsymbol{\omega}$, and the preference for $\mathbf{B}$ and $\mathbf{e}_2$ to be aligned is weak; see ref. [13]. Furthermore, there is a preferred angle of about 40° between $\mathbf{B}$ and $\mathbf{e}_3$, i.e. the eigenvector corresponding to the direction of stretching (see the sketch in Fig. 1). This is in contrast to vortex tubes, which are preferentially perpendicular to both $\mathbf{e}_1$ and $\mathbf{e}_3$, as it is to be expected for a classical vortex tube. The fact that $\mathbf{B}$ can also be oriented in the direction between $\mathbf{e}_2$ and $\mathbf{e}_3$ indicates that the magnetic field occurs typically in the form of ribbon-like structures. This is probably a consequence of the stretching term $B_j \partial_j u_i$ on the right-hand side of the induction equation

$$\frac{\mathrm{D}}{\mathrm{D}t}\langle B_i \rangle = u_{i,j} B_j - u_{j,j} B_i - \eta \nabla^2 B_i, \tag{1}$$

where $\mathrm{D}/\mathrm{D}t = \partial_t + u_j \partial_j$ is the total derivative, commas denote partial derivatives, and summation over double indices is understood. This stretching term seems to play a more important role for the dynamics of $\mathbf{B}$ than the corresponding stretching term $\boldsymbol{\omega}_j \partial_j u_i$ in the equation for $\boldsymbol{\omega}$. This is also seen in the following section where we consider the production rates of the magnetic field in the three principal directions.

Dynamos work partly by the action of stretching of magnetic field lines. This must have some influence on the dynamics of $\mathbf{B}$. Thus, although $\mathbf{B}$ and $\boldsymbol{\omega}$ behave similarly in many respects, it is plausible that it has an enhanced tendency to be tilted into the direction of stretching, or some direction between $\mathbf{e}_2$ and $\mathbf{e}_3$.

2.2. *Generation of flux tubes*

There are essentially two different ways for the magnetic field to be amplified and flux tubes to be generated: one is by random stretching of magnetic field lines and the other one by shear instability of strained magnetic field sheets. In the corresponding context of vorticity production, Vincent and Meneguzzi [17] proposed a simple criterion to distinguish between the two. The equation for the evolution of the average magnetic energy can be obtained by multiplying (1) by B_i and averaging

$$\frac{\mathrm{d}}{\mathrm{d}t}\langle \mathbf{B}^2/2 \rangle = \langle s_{ij} B_i B_j \rangle - \langle \mathbf{B}^2 \nabla \cdot \mathbf{u} \rangle - \langle \eta (\nabla \times \mathbf{B})^2 \rangle. \tag{2}$$

We then define the production rate of magnetic energy as $\lambda^{(B)} = \langle s_{ij} B_i B_j \rangle / \langle \mathbf{B}^2 \rangle$. The same can be done for the production rate of enstrophy, $\lambda^{(\omega)}$. It is useful to compute separately the contributions in the three principal strain directions [17], i.e.

$$\lambda_i^{(B)} = \langle \lambda_i (\mathbf{B} \cdot \mathbf{e}_i)^2 \rangle / \langle \mathbf{B}^2 \rangle, \qquad \lambda_i^{(\omega)} = \langle \lambda_i (\boldsymbol{\omega} \cdot \mathbf{e}_i)^2 \rangle / \langle \boldsymbol{\omega}^2 \rangle. \tag{3}$$

The results are given in Table 1. For the magnetic energy, the production rate in the

Table 1. Production rates of magnetic energy and enstrophy

	1	2	3
$\lambda_i^{(B)}$	−0.092	0.034	0.135
$\lambda_i^{(\omega)}$	−0.077	0.084	0.136
$\lambda_i^{(B)}/\omega_{\mathrm{rms}}$	−0.124	0.046	0.182
$\lambda_i^{(\omega)}/\omega_{\mathrm{rms}}$	−0.104	0.114	0.184

Fig. 3. Flux tube (from red to yellow as field increases) together with the eigenvector $\mathbf{e}_1$ (blue), corresponding to the direction of compression, in a ball with a radius of 4 mesh points around the point of maximum magnetic field strength.

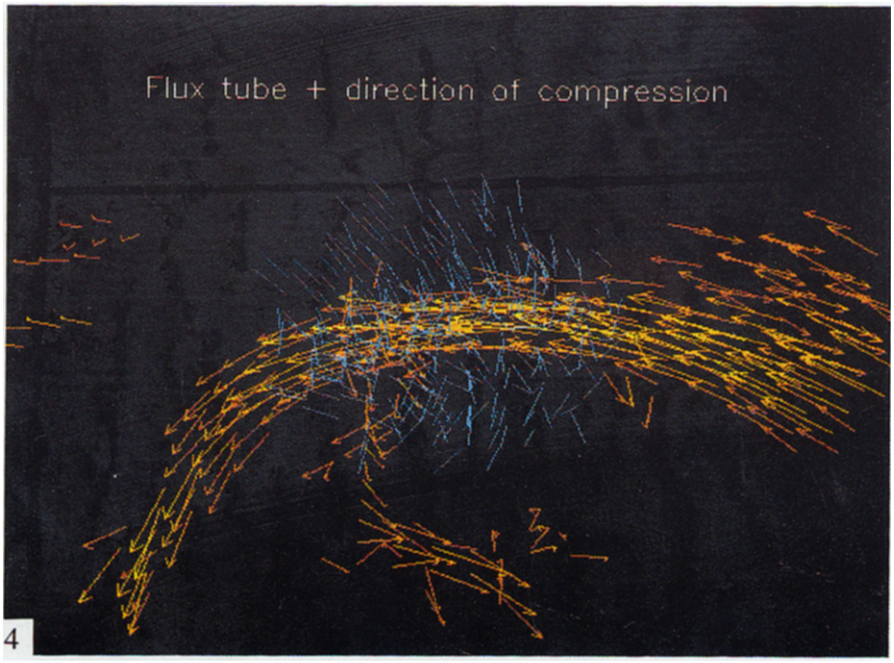

Fig. 4. Flux tube (from red to yellow as field increases) together with the intermediate eigenvector $\mathbf{e}_2$ (blue) in a ball with a radius of 4 mesh points around the point of maximum magnetic field strength.

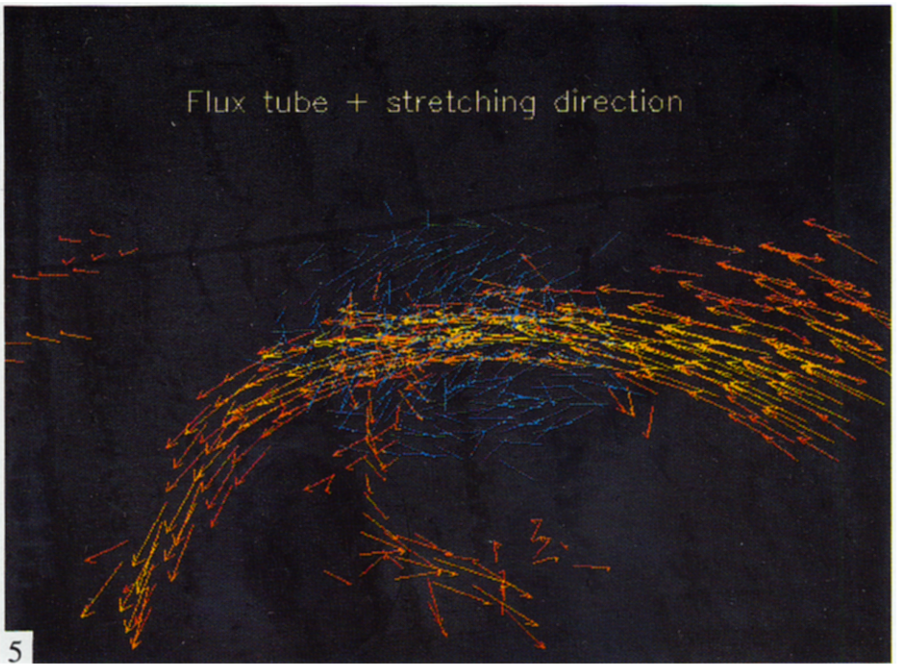

Fig. 5. Flux tube (from red to yellow as field increases) together with the eigenvector $\mathbf{e}_3$ (blue), corresponding to the direction of stretching, in a ball with a radius of 4 mesh points around the point of maximum magnetic field strength.

Fig. 6. Flux tube (from red to yellow as field increases) together with the actual velocity field (blue) in the plane perpendicular to the tube. Note that $\mathbf{u}$ tends to be aligned with the tube.

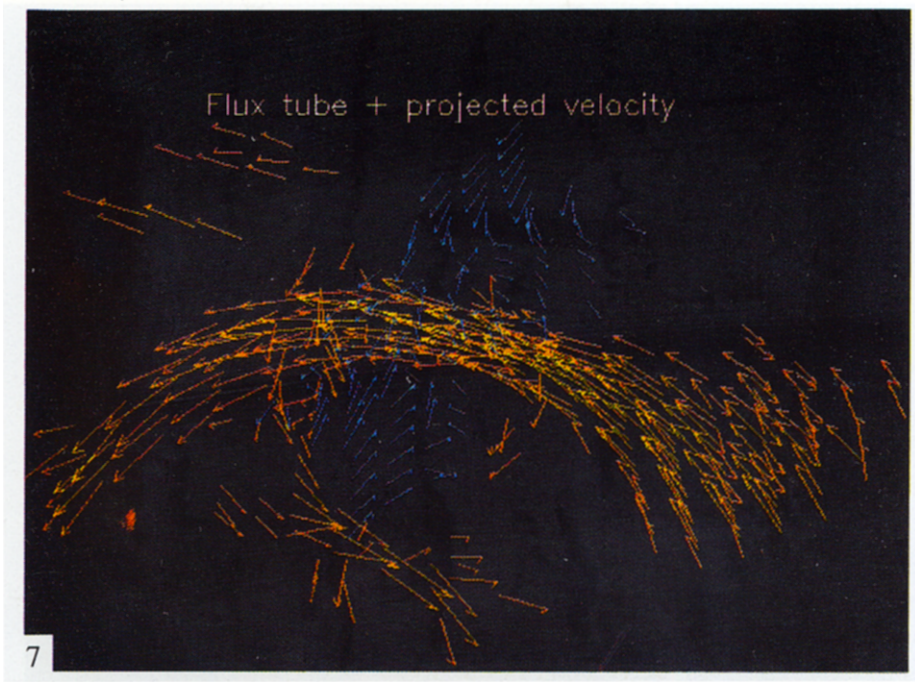

Fig. 7. Flux tube (from red to yellow as field increases) together with the velocity field (blue) projected into the plane perpendicular to the tube.

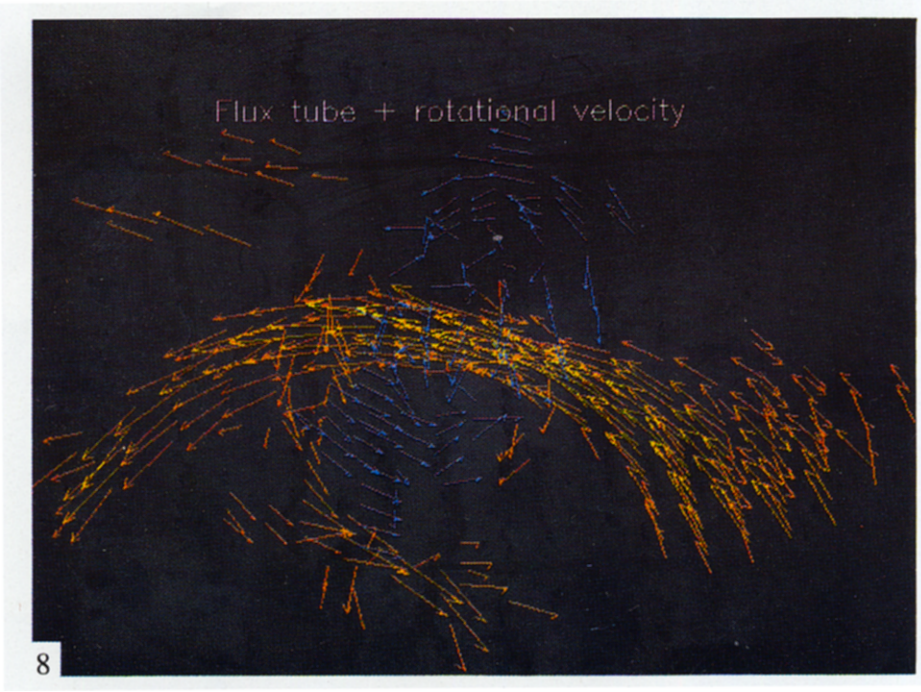

Fig. 8. Flux tube (from red to yellow as field increases) together with the rotational motion (blue) in the plane perpendicular to the tube.

Fig. 9. Flux tube (from red to yellow as field increases) together with the vorticity (blue–green) in a ball with a radius of 4 mesh points around the point of maximum magnetic field strength.

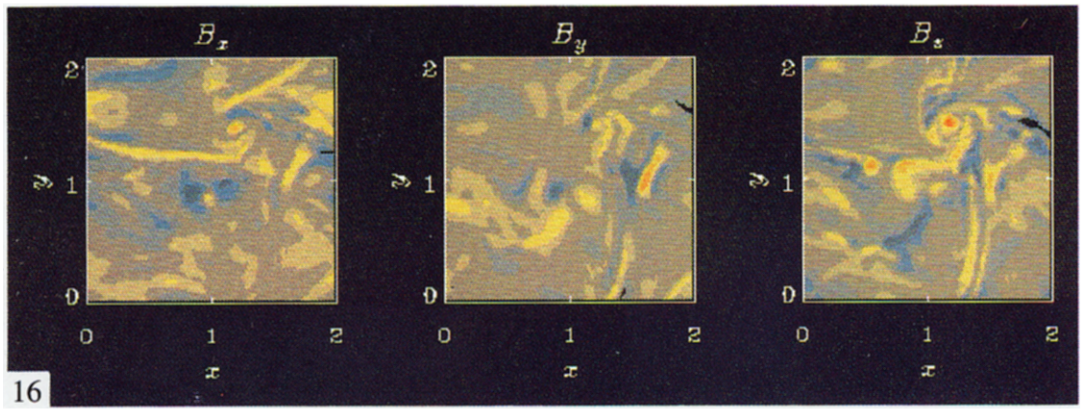

Fig. 16. The three components of **B** in a two-dimensional slice through the box ($z = 1/3$). Orange denotes positive values and blue negative. This slice is used in the following two figures for the computation of the cancellation exponent and generalized magnetic power spectra.

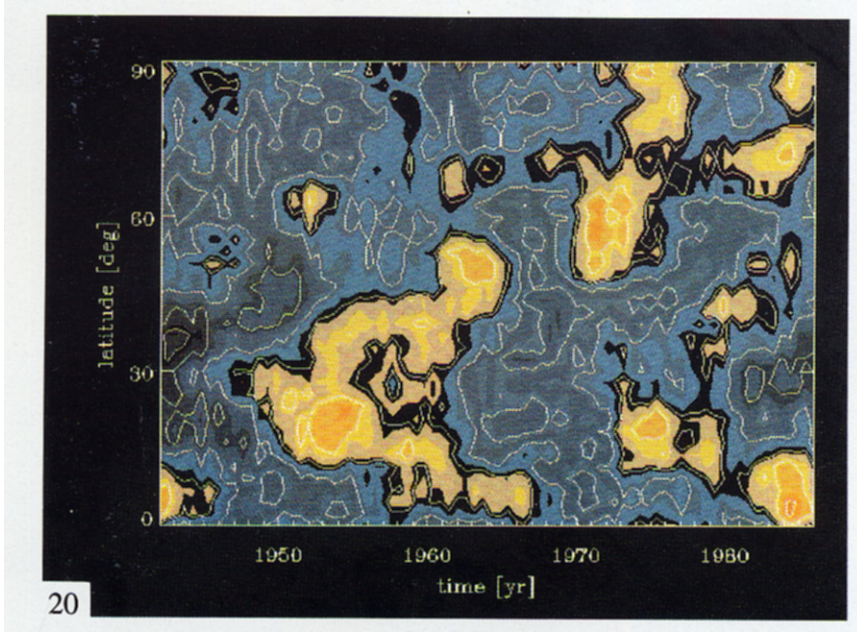

Fig. 20. A numerically generated butterfly diagram of the B_ϕ-field with artificially superimposed noise with a k^{-1} spectrum. Orange denotes positive values and blue negative.

stretching direction is 4.0 times larger than in the intermediate strain direction. This ratio is much larger than the corresponding ratio of about 1.6 for the enstrophy production. This ratio of the values for the enstrophy production is similar to the ratio obtained by Vincent and Meneguzzi [17]. This shows quite clearly that the effect of random stretching of magnetic field lines is rather important in the present dynamo simulations. The magnitude of the production rates of both magnetic energy and enstrophy are comparable to the largest Lyapunov exponent of about 0.08, that was found for the same simulation [21]. The largest production rates, normalized by the rms-value of the strain (i.e. by $\omega_{\rm rms}$), are around 0.2. This is consistent with results from homogeneous turbulence [16].

2.3. *Location of flux tubes*

It is a crucial question to what extent magnetic flux tubes are preferentially generated in stagnation points of the flow, and what the relative importance of straining and rotational motion is. For this purpose we consider the strongest tube in this particular snapshot. We begin by visualizing this tube together with the three eigenvectors. Figures 3–5 confirm that the tube is approximately perpendicular to $\mathbf{e}_1$ and aligned with $\mathbf{e}_2$, but there seems to be an intermediate angle between $\mathbf{B}$ and $\mathbf{e}_3$. Note also that the tube is curved, and that the alignment properties quoted above apply only to the region away from the direction of curvature (upper part in the figures). In the direction of curvature the orientation of the three eigenvectors appears to be more random.

In practice it is difficult to see a well-defined straining motion, as suggested by the eigenvector analysis. In Fig. 6 we display the flux tube together with the velocity field in a plane perpendicular to the tube. Note that there is a significant flow component in the direction of the flux tube, which is also confirmed statistically [13]. A local alignment of $\mathbf{u}$ and $\mathbf{B}$ is expected in MHD turbulence due to the presence of interacting Alfvén waves, and is referred to as the Alfvén effect [22].

Only if the flow component in the direction of the tube is removed, and the average motion in that plane subtracted, does one see a flow reminiscent of a straining motion (see Fig. 7). Of course, the flow consists not only of a straining motion, but also of a rotational motion. In general, we can split the velocity gradient matrix into symmetric and anti-symmetric parts, i.e. $u_{i,j} = s_{ij} + \Omega_{ij}$, where $\Omega_{ij} = -\frac{1}{2}\epsilon_{ijk}\omega_k$. Close to the tube, the rotational motion may be expanded in the form $\Omega_{ij} r_j$, where $\mathbf{r}$ is the radius vector with respect to a reference point on the tube. This rotational component, $\mathbf{u}_{\rm rot} = \frac{1}{2}\boldsymbol{\omega} \times \mathbf{r}$, is isolated in Fig. 8.

The rotational flow is clearly seen at some distance away from the tube. The vorticity corresponding to this motion is directed in the direction of $\mathbf{B}$. This is confirmed by Fig. 9, where the vorticity field is displayed in a ball around the tube. Note, however, that in the immediate surrounding of the tube the vorticity has changed direction and is there oriented antiparallel to the magnetic flux tube.

The presence of a rotational motion around the magnetic flux tubes can be important for stabilizing the tube. This will be discussed in more detail in the following section.

2.4. *Stability of flux tubes*

Soward [23] investigated the stability of a magnetic flux tube in a straining flow with rotation and found a condition $\zeta > 0$ for stability, where

$$\zeta = \lambda_1\lambda_3 + (\tfrac{1}{2}\boldsymbol{\omega}\cdot\mathbf{e}_2)^2. \tag{4}$$

In other words, the tube can be stable if the rotational motion dominates over the straining motion. (Note that $\lambda_1\lambda_3 < 0$.) The same conclusion was reached also by Moffatt *et al.* [24].

A similar analysis has been performed by Klapper and Tabor [25], who quantify the relative importance of straining and rotational motions by the quantity

$$\sigma_2^2 = (\lambda_1 - \lambda_3)^2 - (\boldsymbol{\omega}\cdot\mathbf{e}_2)^2. \tag{5}$$

If σ_2^2 is positive the magnetic field can grow exponentially. The two quantities are related via $\sigma_2^2 = (\lambda_1 + \lambda_3)^2 - 4\zeta$.

Locally, the stability of the magnetic field is governed by the eigenvalues of the operator on the right-hand side of (1). Neglecting diffusion and the $\nabla\cdot\mathbf{u}$ term, we can get some preliminary information by considering the eigenvalues of the velocity gradient matrix $u_{i,j}$. In the frame spanned by the principal strain axes, we can write

$$u_{i,j} = \begin{pmatrix} \lambda_1 & -\frac{1}{2}\boldsymbol{\omega}\cdot\mathbf{e}_3 & \frac{1}{2}\boldsymbol{\omega}\cdot\mathbf{e}_2 \\ \frac{1}{2}\boldsymbol{\omega}\cdot\mathbf{e}_3 & \lambda_2 & -\frac{1}{2}\boldsymbol{\omega}\cdot\mathbf{e}_1 \\ -\frac{1}{2}\boldsymbol{\omega}\cdot\mathbf{e}_2 & \frac{1}{2}\boldsymbol{\omega}\cdot\mathbf{e}_1 & \lambda_3 \end{pmatrix} \approx \begin{pmatrix} \lambda_1 & 0 & \frac{1}{2}\boldsymbol{\omega}\cdot\mathbf{e}_2 \\ 0 & \lambda_2 & 0 \\ -\frac{1}{2}\boldsymbol{\omega}\cdot\mathbf{e}_2 & 0 & \lambda_3 \end{pmatrix}, \tag{6}$$

where the approximation (second term) is only valid in those places where there is good alignment between $\boldsymbol{\omega}$ and $\mathbf{e}_2$. One of the three eigenvalues of $u_{i,j}$ is $s_1 = \lambda_2$, but this corresponds to growth or decay in the direction of the tube (provided $\mathbf{B}$ is also aligned with $\mathbf{e}_2$). If $|\zeta| \ll |\lambda_1 + \lambda_3|$, we can write the other two eigenvalues as $s_2 = \lambda_1 + \lambda_3$ and $s_3 = \zeta/(\lambda_1 + \lambda_3)$. Thus, if a magnetic flux tube is aligned with $\mathbf{e}_2$, and if $\lambda_1 + \lambda_3 < 0$, then the tube would be confined if $\zeta > 0$ [23].

In order to check the possibility of tubes being located in stagnation points and stabilized by a sufficiently strong rotational component, we present in Fig. 10 the statistics of various quantities for discrete windows of $|\mathbf{B}|$. This allows us to distinguish between regions of strong magnetic field (usually associated with flux tubes) and weak field (corresponding to the background). If flux tubes are indeed located in the surroundings of stagnation points, we would expect that the flow component perpendicular to the magnetic field, $\mathbf{u}_\perp = \mathbf{u} - (\mathbf{u}\cdot\mathbf{B})/|\mathbf{B}|$, is small in those places. In Fig. 10 we compare the $|\mathbf{B}|$-dependencies of $(\mathbf{u}_\perp^2)^{1/2}$ and $|\mathbf{u}_\perp|_{\max}$ with those of $(\mathbf{u}^2)^{1/2}$ and $|\mathbf{u}|_{\max}$. As $|\mathbf{B}|$ increases, $(\mathbf{u}_\perp^2)^{1/2}$ decreases, which is compatible with the idea of a stagnation point. This is even better seen in the dependence of $|\mathbf{u}_\perp|_{\max}$, which approaches almost zero for the maximum magnetic field. On the other hand, there remains a significant flow component in the direction of the magnetic field, as seen in the dependencies of $(\mathbf{u}^2)^{1/2}$ and $|\mathbf{u}|_{\max}$. This may be associated with the Alfvén effect mentioned in Section 2.3.

In Fig. 10 we have also plotted the $|\mathbf{B}|$-dependence of the average of the stability parameter ζ. For most values of $|\mathbf{B}|$, ζ is on average negative indicating that magnetic flux

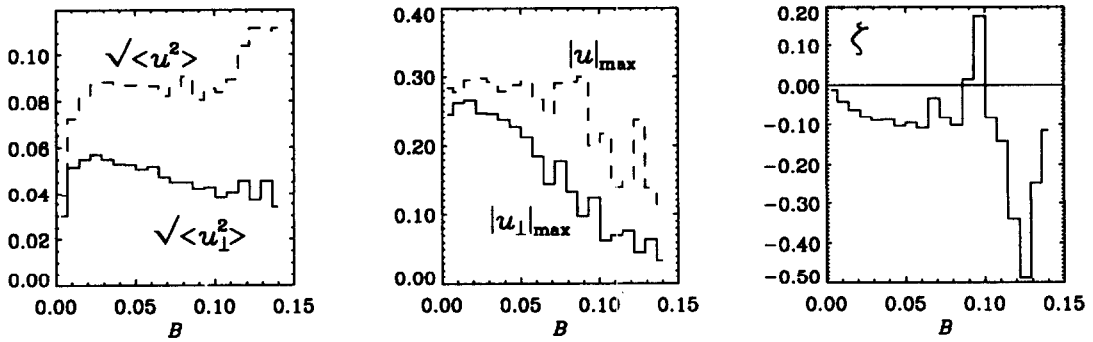

Fig. 10. Statistical analysis of the rms and maximum values of $|\mathbf{u}|$ (dotted) and $|\mathbf{u}_\perp|$ (first and second panel) and the average value of ζ (third panel) for discrete windows of $|\mathbf{B}|$.

field structures are generally unstable. This is not surprising, because from video animations of the field we know that flux tubes come and go, with a typical life time of only a few turnover times. Nevertheless, for a narrow range of intermediate $|\mathbf{B}|$ values the average value of ζ does become positive. Thus, it seems that once the magnetic field has reached a certain threshold value of $|\mathbf{B}| \approx 0.7|\mathbf{B}|_{\max} \approx 6\langle \mathbf{B}^2 \rangle^{1/2}$, the tubes can become locally stable. However, when the field becomes even stronger, the tube will become unstable again.

After having discussed the formation of individual flux tubes, we now turn to the question of their geometrical structure and consider in the following their fractal dimension.

3. FRACTAL DIMENSION OF FLUX TUBES

The fractal dimension of level sets of temperature, concentration of chemicals, and of the magnitude of the vorticity has attracted attention since Mandelbrot [26] associated intermittency in fluid turbulence with fractal properties of the dissipation field. Constantin and Procaccia [27] established the estimate $D \approx 2.7$ for the fractal dimension of level sets of vorticity, based on the Navier–Stokes equations. This result is consistent with data of three-dimensional simulations of Navier–Stokes turbulence [28]. Similar estimates have also been obtained for level sets of the magnetic field in a dynamo simulation [14]. However, in those cases where MHD turbulence is dominated by interacting Alfvén waves (the Alfvén effect), Biskamp [29] derived $D = 2.75$ for level sets of the modulus of the current, $|\mathbf{J}|$. He confirmed this using high resolution simulations of two-dimensional MHD turbulence.

Here we reconsider estimates of the fractal dimension of $|\mathbf{B}|$ and $|\mathbf{J}|$ in a MHD dynamo simulation. It is important whether or not the lower overshoot layer is included in the analysis. In ref. [14] the lower overshoot layer has been removed and the remaining field in the convection zone (with aspect ratio 2:2:1) has been replicated in order to fill a cube with equal side walls (2:2:2). This resulted in rather bad scaling in the sense that the local dimension $D(r)$ at length scale r did not show any plateau. Below we present the results including the data in the lower, stably stratified region. The scaling for both the magnetic field and the electric current is now much better. There is a clear transition from two-dimensional behavior at small scales ($r \approx 1$ mesh size) to fractal behavior at larger scales ($r \approx 10 - 30$ mesh sizes). In the intermediate range the fractal dimensions of the two fields are compatible with $D = 2.7$. However, the accuracy is insufficient to distinguish between the values 2.70 and 2.75. It should be noted, however, that in the dynamo simulations the flow does not seem to be governed by the Alfvén effect, and therefore $D \approx 2.7$ would be expected for Kolmogorov turbulence.

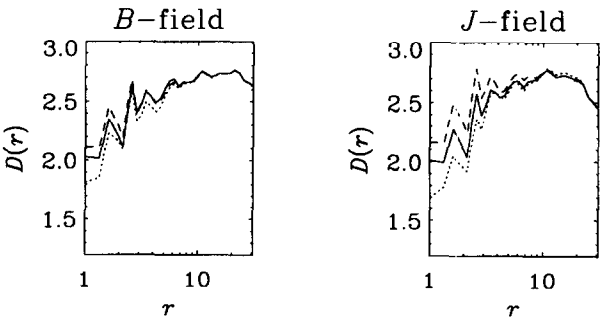

Fig. 11. The scaling of the fractal dimension $D(r)$ for level sets of $|\mathbf{B}|$ and $|\mathbf{J}|$ (solid lines). Dotted and dashed lines refer respectively to smaller and larger window widths of the values of $|\mathbf{B}|$ and $|\mathbf{J}|$ that have been included in the level set.

The fractal dimension of level sets of $|\mathbf{B}|$ and $|\mathbf{J}|$ have been determined using the Grassberger–Procaccia algorithm [30]. In fact, there is a whole spectrum of different dimensions [31], including, for example, the Hausdorff dimension D_0, the information dimension D_1, and the correlation dimension D_2 (which is the dimension considered above). The values of these different dimensions are only different if the set contains singularities [32]. Level sets do not contain singularities (the density of points is limited by the mesh), and therefore level sets do not show multifractal behaviour. A different situation arises if we consider instead the continuous field of the vorticity or the magnetic field. In the following section we first explain the basic tools for doing this and then illustrate the difference between the two rather different fractal aspects of the field.

4. SCALE DEPENDENCE OF THE MAGNETIC FIELD

4.1. *Generalized dimensions*

The generalized dimensions, D_q, of the $|\mathbf{B}|$-field are important, because they provide a description of the magnetic field structure, and can thus be used to compare the results of different simulations [33]. Furthermore, the local value of $D_q(r)$ for $q \to \infty$ gives information about the sharpness of the strongest 'near-singularities' of the $|\mathbf{B}|$-field [32]. Such near-singularities behave approximately like $|\mathbf{r} - \mathbf{r}_0|^{D_\infty - 3}$, although the peak itself must always be smooth. This kind of profile has also been confirmed by looking at the cross-sections of the magnetic field in actual simulations [14]. A full picture of the near-singular structures can only be obtained when all D_qs are known. We return to this in the following subsection.

In order to estimate the 'local' generalized dimensions, $D_q(r)$, one divides the space into $N(r)$ boxes of size r and subvolume $V_i(r)$ with $i = 1, \ldots, N(r)$, and computes the scaling of the generalized correlation integral, $C_q(r) = \sum_i p_i(r)^q$, where the weight or normalized magnetic field strength in each box is

$$p_i(r) = \frac{\int_{V_i(r)} |\mathbf{B}| \, \mathrm{d}^3x}{\int_V |\mathbf{B}| \, \mathrm{d}^3x}. \tag{7}$$

The 'local' generalized dimension is then given by

$$D_q(r) = \frac{1}{q-1} \frac{\mathrm{d} \ln C_q(r)}{\mathrm{d} \ln r} \tag{8}$$

(for further details on the computation see ref. [14]).

The same analysis has also been carried out for the magnitude of the vorticity in hydrodynamical simulations of forced turbulence. For example, the data of Vincent and Meneguzzi [12] give $D_\infty \approx 1$ at small scales close to $r = l_d$ [14], where l_d is the dissipative Kolmogorov cutoff scale. This implies that the strongest near-singularities in this field behave like $|\mathbf{r} - \mathbf{r}_0|^{-2}$. For the magnetic field the situation is qualitatively similar, although the near-singularities are less strong, which may be related to insufficient numerical resolution. In the MHD simulation, the Reynolds number based on the Taylor microscale, $\lambda = (\langle \mathbf{u}^2 \rangle / \langle \boldsymbol{\omega}^2 \rangle)^{1/2}$ is $\mathrm{Re}_\lambda \approx 30$ ($\boldsymbol{\omega} = \nabla \times \mathbf{u}$ is vorticity). In this run the Rayleigh number has been pushed to the limit, and the smallest structures are therefore only poorly resolved. This may be the reason for the relatively weak appearance of near-singularities compared to the hydrodynamical case. Indeed, for small values of r, $D_q(r)$ does not show a tendency

for approaching the embedding dimension $d = 3$ at the scale of the mesh (see also Section 4.3 and Fig. 14). A local dimension close to d is always to be expected at the smallest scales where the field ought to become smooth.

In the intermediate (inertial?) range there is no good scaling of D_1, but there is a crossover to $D_1 \to 3$ at large scales. This is the case even for the 240^3 simulation of Vincent and Meneguzzi [12] where $\mathrm{Re}_\lambda \approx 160$. This shows that truly multifractal behavior is only to be expected for much larger Reynolds numbers. Indeed, Meneveau and Sreenivasan [34] find good scaling in the inertial range for the flow in the atmospheric surface layer ($R_\lambda = 1500$). Using Taylor's hypothesis, they estimated the local dissipation from a time series ($d = 1$) and found $D_1 = 0.7$, corresponding to 2.7 for the three-dimensional case. This is also the value that is theoretically expected for the level sets of vortex tubes [27], suggesting that D_1 of the field and D of level sets are indeed connected to each other. Nevertheless, it is important to distinguish between the fractal dimension of level sets in the inertial range and the dimensions D_q at small scales. Whilst the latter measures the local sharpness of cross-sections through a vortex tube, the former measures the degree of wrinkling of the tube at large scales. These two quite different aspects are illustrated in the following sketch (Fig. 12).

The wrinkling of vortex tubes may reflect the presence of concentrations of curvature and torsion which, in turn, could be the result of solitons propagating along those tubes [35–37]. In the following we focus attention on various statistical properties of flux tubes.

4.2. *The $f(\alpha)$ spectrum*

The multifractal aspects of turbulence may be characterised by the $f(\alpha)$ spectrum. Its role in MHD turbulence has been explained in the review of Biskamp [38]. Qualitatively, $f(\alpha)$ is the dimension of the set of points, where the field scales locally like $|\mathbf{r} - \mathbf{r}_0|^{\alpha-3}$, i.e. where the pointwise dimension is equal to α [32]. The $f(\alpha)$ spectrum is usually computed from the generalized dimensions via a Legendre transform;

$$\alpha(q) = \frac{\mathrm{d}\tau}{\mathrm{d}q}, \qquad f(\alpha) = q\alpha(q) - \tau(q), \tag{9}$$

where $\tau(q) = (q-1)D_q$. This method has been applied to simulations of MHD turbulence [14].

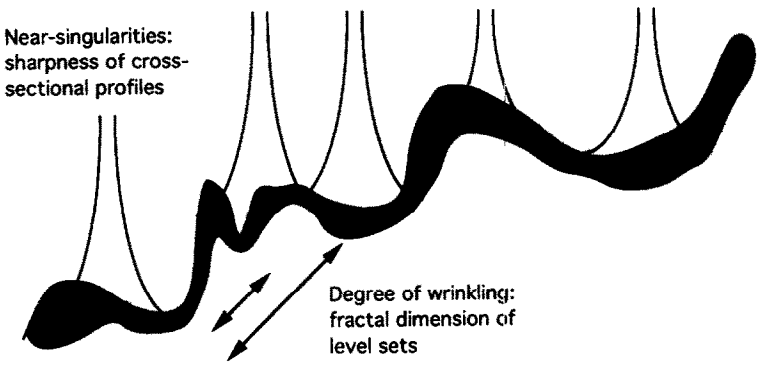

Fig. 12. Sketch illustrating the two aspects of tubes: (i) the degree of wrinkling of the entire tube geometry, and (ii) the sharpness of their cross-sections.

It should be noted, however, that we only have truly multifractal behavior if there is good scaling of C_q. On the other hand, if one assumes scaling behavior, $f(\alpha)$ can be readily determined directly from the statistics of the $p_i(r) \sim r^{\alpha_i}$ via the histogram $N(\alpha)$ of the pointwise dimensions,

$$\alpha_i = \ln p_i(r)/\ln r. \tag{10}$$

This method is due to Chhabra and Jensen [39], and has recently been adopted by Lawrence *et al.* [40] for the analysis of solar magnetograms. The histogram $N(\alpha; r)$ should scale like

$$N(\alpha; r) = \phi(r) r^{-f(\alpha)}, \tag{11}$$

and so we can determine $f(\alpha) = -\ln(N/\phi)/\ln r$, where $\phi(r)$ is a slowly varying function [40].

In Fig. 13 we compare the resulting $f(\alpha)$ spectra using the two different methods. In practice, the direct method appears to be slightly less convincing than the method via the generalized dimensions in that certain criteria such as $\max(f) = D_0 = 3$ and $\alpha - f(\alpha) \geqslant 0$ are not satisfied to sufficient accuracy. If $f(\alpha)$ is determined directly, the dependence of D_q on q can still be evaluated from $f(\alpha)$ via the inverse Legendre transform

$$q = \mathrm{d}f/\mathrm{d}\alpha, \qquad \tau = q\alpha - f(\alpha). \tag{12}$$

The result is shown in Fig. 13(c).

The left-hand branch of the f(a) spectrum corresponds to positive values of q and gives the fractal dimension of the set of points on which the field behaves locally like $|\mathbf{r} - \mathbf{r}_0|^{\alpha-3}$. For example, the strongest near-singularities in the field have $\alpha \approx 2.5$ with $f(\alpha) \approx 1$. This means that those near-singularities lie on a one-dimensional set, corresponding to tube-like structures.

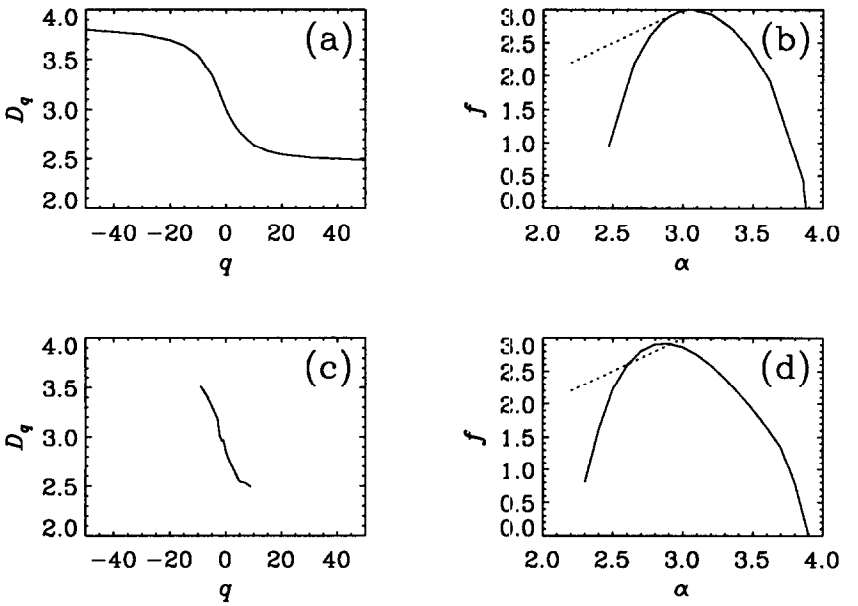

Fig. 13. The dependence of D_q on q (a), and the corresponding $f(\alpha)$ spectrum (b), using the method via the generalized dimensions. In (c) and (d) the resulting plots are given by using the histogram method.

In this section we used the standard definition of a measure, as opposed to so-called signed measures. Signed measures have recently attracted some attention because of their physical significance in the dynamo problem. This will be considered in the next section.

4.3. *Signed measures and the cancellation exponent*

There has been recent interest in 'signed' measures [33, 40, 41]. Signed measures are obtained by averaging either **B** (instead of $|\mathbf{B}|$ or $\mathbf{B}^2$), or one of the field components, over squares or boxes of size r. Thus, the signed measure of the magnetic field corresponds to the magnetic flux at scale r. For astrophysical dynamos it is essential to generate magnetic flux at large scales. This may be part of the reason why signed measures are considered to be important. In ref. [40] the signed measure $\mu_i(r)$ is normalized such that $\sum_i \mu_i = 1$, where

$$\mu_i(r) = \frac{\left| \int_{V_i(r)} B \, dV \right|}{\sum_i \left| \int_{V_i(r)} B \, dV \right|}, \tag{13}$$

and B stands for one of the three components of the magnetic field. In Fig. 14 we compare the result for unsigned and signed measures for the B_z component of the magnetic field. It turns out that the dimension for the unsigned measures is typically smaller than for signed ones.

Strictly speaking, a signed 'measure' is actually not a measure, because the measure $\mu(A_1 + A_2)$ of the field in two areas, A_1 and A_2, is not equal to the sum of the measures $\mu(A_1) + \mu(A_2)$, as it has to be the case for ordinary measures. However, if we divide the space into areas A_+ and A_-, where B_z is either positive or negative, we have $\mu(A_+ + A_-) = \mu(A_+) - \mu(A_-)$. This suggests that, if we are to consider multifractal properties of the signed flux, we should compute the scaling separately in regions of positive and negative B_z. In practice this is done by computing, as usual, the generalized dimensions using (13) and (8), but setting the field with either negative or positive sign to zero. The result is shown in Fig. 15. The curves for $\mu(A_+)$ and $\mu(A_-)$ look roughly similar. Furthermore, the shape of the curves for $q = 1$ is similar as for the usual unsigned measure (Fig. 14), but the local codimension, $d - D_1(r)$, is now about twice as big as for the unsigned measure.

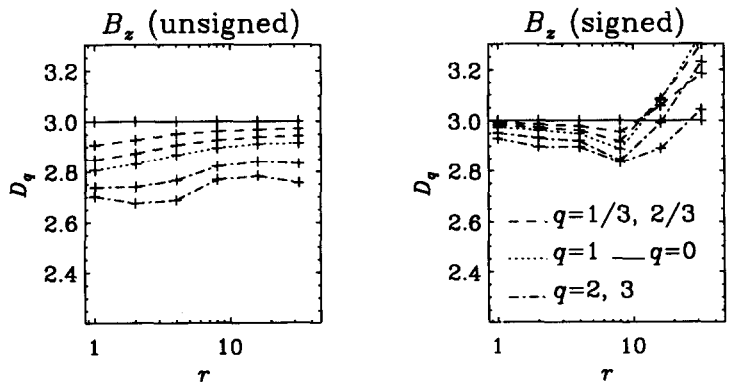

Fig. 14. The scaling behavior of $D_q(r)$ using unsigned and signed measures of the B_z component of the magnetic field.

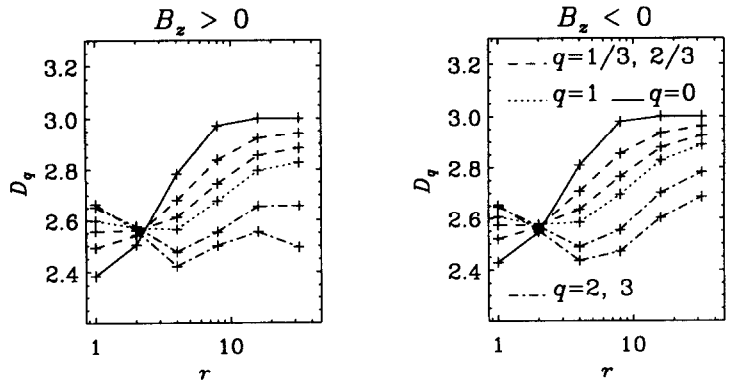

Fig. 15. The scaling behavior of $D_q(r)$ using the measures $\mu(A_+)$ and $\mu(A_-)$ of the B_z component of the magnetic field.

The normalization used in equation (13) is r-dependent. This is avoided in the definition used in refs [33, 41];

$$m_i(r) = \frac{\left|\int_{V_i(r)} B\,\mathrm{d}V\right|}{\left|\int_V B\,\mathrm{d}V\right|}, \tag{14}$$

but now $\chi(r) = \sum_i m_i(r) \neq 1$. The scaling of the cancellation exponent κ [41] may be determined via

$$\kappa(r) = -\frac{\mathrm{d}\ln\chi(r)}{\mathrm{d}\ln r}. \tag{15}$$

In order to generalize $\chi(r)$ in a convenient way we define

$$\mathcal{B}_q(r) = \langle|\langle\mathbf{B}\rangle_r|^q\rangle^{1/q}, \tag{16}$$

where $\langle\ldots\rangle_r$ denotes an average over a box of scale r, and $\langle\ldots\rangle$ is an average over the entire computational volume. The total magnetic energy is proportional to $\langle\mathbf{B}^2\rangle \equiv \mathcal{B}_2^2(0)$. It is important to note that $\langle\mathbf{B}^2\rangle$ can be significantly underestimated if the magnetic field continues to be intermittent and nonsmooth down to the smallest scales resolved. This is a particular problem when data of observations are analysed. The r-dependence of $\mathcal{B}_2(r)$ can then in principle be used to extrapolate to the limit of perfect resolution, $r \to 0$.

The scalings of $\mathcal{B}_1$ and χ are identical, i.e. $\mathrm{d}\ln\chi/\mathrm{d}\ln r = \mathrm{d}\ln\mathcal{B}_1/\mathrm{d}\ln r$. It is straightforward to define generalized cancellation exponents

$$\kappa_q(r) = -\frac{\mathrm{d}\ln\mathcal{B}_q(r)}{\mathrm{d}\ln r}. \tag{17}$$

The exponent κ_2 can be used to characterize the dependence of $\langle\mathbf{B}^2\rangle$ on the Reynolds number. Assuming that the magnetic field is concentrated on the scale of the skin depth, $r \sim R_m^{1/2}$, Bertozzi *et al.* [42] were able to relate the scaling exponent n in the relation $\langle\mathbf{B}^2\rangle \sim R_m^n$ to $\kappa = \kappa_1$ and D_2. Following the definition (17), we see immediately that $n = \kappa_2$. In the following, however, we point out that the assumption of power-law scaling is not in general valid.

In order to facilitate comparison with magnetic power spectra (see the following section) we use here, as well as in the following section, a two-dimensional slice through the box ($z = 1/3$), for which the **B**-field is shown in Fig. 16.

In Fig. 17 we plot $\kappa_q(r)$ for different values of q. Note that $\kappa_q(r)$ does not show power-law behavior. This is at first surprising because the power spectrum for the magnetic energy does show a small intermediate (inertial?) range with a power law compatible with a k^{-1} spectrum. Vainshtein *et al.* [43] pointed out that the cancellation exponent of the vorticity, $\boldsymbol{\omega} = \nabla \times \mathbf{u}$, is related to the structure function ζ_1 of velocity increments which, in turn, is related to the power spectrum of $\mathbf{u}$, i.e. to the kinetic energy. Thus, the cancellation exponent of $\mathbf{B}$ should rather be compared with the structure function or the power spectrum of the magnetic vector potential $\mathbf{A}$, since $\mathbf{B} = \nabla \times \mathbf{A}$. Alternatively, we may compare the power spectrum of $\mathbf{B}$ with the cancellation exponent of $\mathbf{J} = \nabla \times \mathbf{B}/\mu_0$. This is done in the second panel of Fig. 17. Note that for $q \leqslant 1$ there is indeed a tendency for κ_q to level off at large scales, indicating that power-law scaling is possible.

In conclusion, the numerical results for the cancellation exponent of the magnetic field show no good scaling, even though the power spectra do show some weak evidence of an inertial range (see next section). It is possible that the lack of scaling is due to the relatively short range of length scales that is available in current three-dimensional simulations. For practical purposes it is therefore useful to know that in spectral-space scaling may be found at relatively low Reynolds numbers, while in real space there is no scaling for those Reynolds numbers. In the following section we elaborate on scaling properties in spectral space and on the possible connection with scaling in real space.

4.4. *Generalized power spectra*

Instead of partitioning the domain into boxes, as we did in the previous sections, we may alternatively use a spectral decomposition. Because of the inhomogeneity in the vertical direction we have restricted ourselves to two-dimensional spectra in a horizontal plane in the upper third of the box ($z = 1/3$), i.e. we use $\hat{\mathbf{B}}(\mathbf{k}) = \int \mathbf{B}(x, y, z_0, t_0) \exp[i(k_x x + k_y y)] \, dx \, dy$, and compute generalized power spectra

$$M_q(k) = \int_0^{2\pi} |\hat{\mathbf{B}}(\mathbf{k})|^q k \, d\phi_k, \tag{18}$$

where the $k \, d\phi_k$ integration is over shells of constant $k = |\mathbf{k}|$, and k and ϕ_k are cylindrical polar coordinates in $\mathbf{k}$-space. Note that $M_2(k)$ is the usual spectral magnetic energy. In the inertial range we expect power-law behavior and, since for $q = 0$ the integrand is proportional to k, i.e. $M_0(k) \sim k^1$, it is sensible to write

$$M_q(k) \sim k^{1-qn_q}. \tag{19}$$

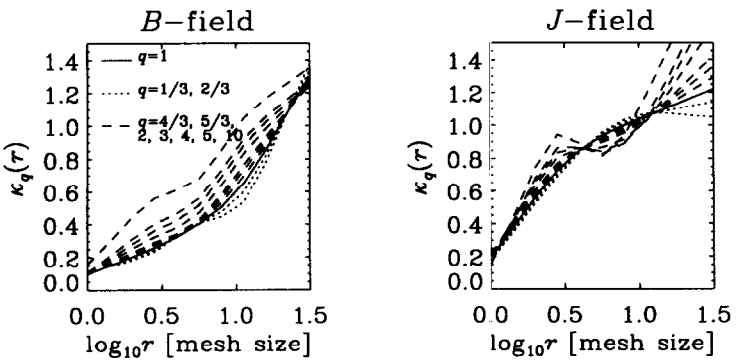

Fig. 17. The dependence of $\kappa_q(r)$ on r for different values of q using the signed measure of $\mathbf{B}$ (left) and $\mathbf{J}$ (right).

In Fig. 18 we show the local slope, $\mathrm{d}\ln M_q(k)/\mathrm{d}\ln k$, as a function of wave number k. We also display the dependence of the scaling exponent n_q on q. Because of the relatively small resolution an inertial range can hardly be expected. Nevertheless, for intermediate wave numbers the local slope tends to show a small plateau with $n_2 \approx 1$, corresponding to $M_2(k) \sim k^{-1}$. Note that deviations from the $n_q \approx 1$ scaling are relatively weak, i.e. there is no strong 'multispectral' behavior. For comparison, Kolmogorov scaling with a $k^{-5/3}$ spectrum corresponds to $n_2 = 4/3$.

In order to investigate the correspondence between power spectra and the cancellation exponent further, we now compute $\kappa_q(r)$ for artificially generated data with random phases and a given power spectrum, k^ν. For this experiment we use a two-dimensional mesh with 256×256 points. It turns out that, again, there is no power-law behavior, i.e. $\kappa_q(r)$ does not show a plateau. Instead, we find that to a good approximation

$$\kappa_q(r) = ar^b, \tag{20}$$

where a and b are functions of ν which are shown in Fig. 19. For the artificially generated data this dependence is independent of q. Note that for $\nu = -1$, $\log_{10} a = -0.6$ and $b = 0.5$, which is in rough agreement with the case depicted in Fig. 17. Furthermore, for different q the value of κ_q is almost the same, i.e. there is no 'multiscaling' in the

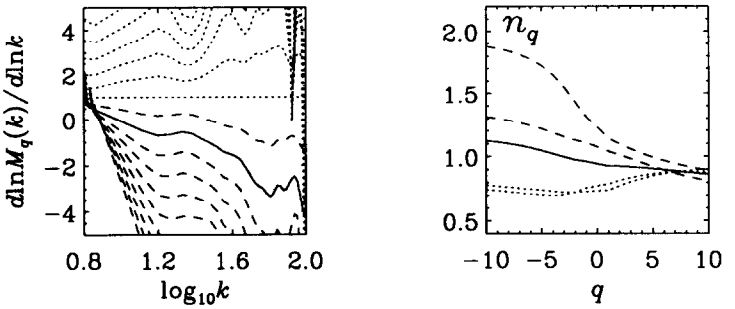

Fig. 18. *Left:* The local slope of the generalized power spectrum. The solid line is for $q = 2$, dotted lines for $-10 \leq q \leq 0$, and dashed lines for $0 < q \leq 10$. (Note that the largest wave number is $\pi/\Delta x \approx 100$.) *Right:* The scaling exponent n_q (solid line) taken as the average local slope around $\log_{10} k_m = 1.4$. The dotted and dashed lines indicate the local slopes for $k < k_m$ and $k > k_m$, respectively, and may be used to estimate the quality of scaling.

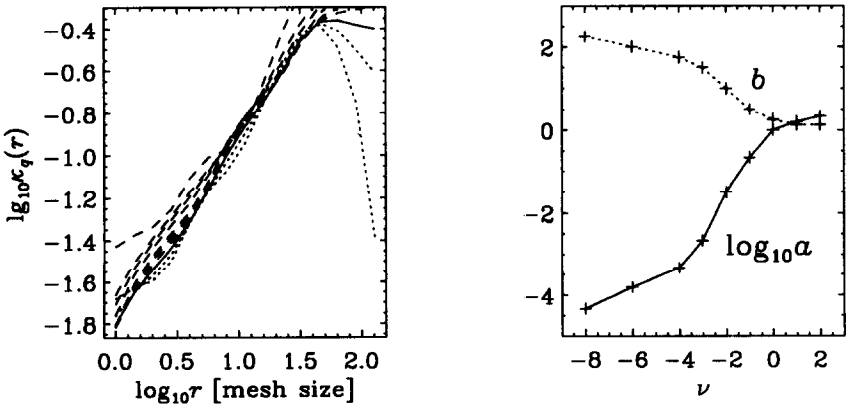

Fig. 19. *Left:* The local value of $\log_{10} \kappa_q(r)$ for artificially generated data with a k^ν power spectrum for $\nu = -1$. *Right:* The fit parameters a and b as a function of ν.

artificially generated data. Only white noise, i.e. $\nu = 0$, leads to a constant slope with $\kappa_q = 1$.

It is important to note that the k^{-1} spectrum for the magnetic energy that is seen in the simulations, and which has been predicted especially in the context of dynamo action with an inverse cascade [22], is of deep importance for the solar dynamo. Qualitatively, the steepness of the spectrum determines the importance of large scale fields relative to small scale fields. This is illustrated in the following section.

5. IMPLICATIONS CONCERNING THE SOLAR DYNAMO

The purpose of this section is to discuss the role and importance of small-scale magnetic fields in the solar dynamo. On the other hand, the solar magnetic field shows rather regular behavior, including the 11-year cycle, the equatorial migration of the magnetic field belts, and the systematic orientation of these field belts that reverses after 11 years. On the other hand, this process is believed to originate from the turbulence motions, that are intrinsically irregular. This appears paradoxical. Put into a more general context one might ask the question as to how strong the irregular small-scale magnetic field can be without losing the appearance of an underlying structure of a large-scale magnetic field.

In order to address this question, we now make an experiment using a large-scale magnetic field pattern (in space and time) and add statistical noise with a k^{-1} power spectrum, that was found to be consistent with the simulations (previous section). The large-scale magnetic field pattern is derived from a mean-field model of the solar dynamo. A few words concerning this model are here in order. It is commonly believed that the large-scale magnetic field seen in the sun is related to the inverse cascade of the magnetic helicity that leads to a gradual increase or maintenance of the magnetic energy at large scales [22]. Qualitatively the same process is realised in so-called α-effect dynamos [1, 44] where, however, only the large-scale magnetic field is solved for explicitly, and the effects of the small-scale fields have been subsumed into the α-effect and the turbulent magnetic diffusion. Recently progress has been made by applying consistently derived expressions for the full α and η tensors to a model of the solar overshoot layer [45]. We now use this model to address the question of an upper limit on the strength of magnetic fluctuations, $\mathbf{B}'$, that are still compatible with the appearance of a large scale magnetic field, $\langle \mathbf{B} \rangle$.

We use a butterfly diagram of the B_ϕ-field from this model and add noise with a k^{-1} power spectrum. The noise has an exponential distribution function and is generated on a (θ, ϕ, t)-mesh, where θ is colatitude, ϕ longitude, and t time, with a resolution of $2.3° \times 2.3° \times 0.5$ yr. The energy of the noise, $\langle \mathbf{B}'^2 \rangle$, has been scaled relative to the energy of the mean field, $\langle \mathbf{B} \rangle^2$, such that

$$\langle \mathbf{B}'^2 \rangle / \langle \mathbf{B} \rangle^2 \approx 100. \tag{21}$$

The resulting field $\mathbf{B} = \langle \mathbf{B} \rangle + \mathbf{B}'$ is then averaged over ϕ, and a running mean over 4 years is adopted to smooth the data. Thus, we treat our numerically generated data very much like observers would do. The result is shown in Fig. 20.

Note that the basic features of an equatorward migration at low latitudes and a poleward migration at high latitudes can still be distinguished from the superimposed noise. We thus argue that a noise level of 100:1 relative to the regular mean field component is still compatible with the observations. In reality, the noise level might be rather lower than that, because it is also observed that strong, individual bipolar regions (that are not subject to averaging) are always systematically oriented. The usual interpretation is that such fields originate from deeper layers (probably the overshoot layer) where the magnetic fluctuations are weak and the field strong.

6. CONCLUSIONS

Numerical simulations of three-dimensional MHD convection may be used to improve our understanding of the solar dynamo. At the same time, such simulations exhibit an enormous amount of interesting turbulence physics. Due to the presence of rotation, stratification, and overshoot layers, a variety of aspects can be addressed. In the present paper we have focussed on different ways to characterize the geometry of magnetic flux tubes in such a dynamo simulation, and to describe scale-dependent properties of the magnetic field. In addition to the recently developed concept of signed measures, generalized power spectra of the magnetic field may be used to characterize such aspects. Investigating the development of the magnetic power spectrum is indeed a convenient way to detect an inverse magnetic cascade, which is a key issue in understanding the development of the large-scale magnetic field of the sun. Unfortunately, current MHD simulations are as yet not realistic enough to attain sufficiently large an inertial range and to establish power-law behavior. However, it seems that the magnetic 'noise', associated with MHD turbulence and a magnetic power spectrum of k^{-1} (or even steeper) is still compatible with the appearance of a large-scale magnetic field as is seen on the sun.

Acknowledgements—The National Center for Atmospheric Research is sponsored by the National Science Foundation. I am grateful to Bob Kerr, Isaac Klapper, David Moss, Sasha Ruzmaikin, Daniel Segel, Dmitry Sokoloff, Andrew Soward, Samuel Vainshtein and Alain Vincent for discussions, suggestions, and/or comments on the manuscript.

REFERENCES

1. F. Krause and K.-H. Rädler, *Mean-field Magnetohydrodynamics and Dynamo Theory*. Akademie-Verlag, Berlin (1980).
2. P. A. Gilman, Dynamically consistent nonlinear dynamos driven by convection in a rotating spherical shell: II. Dynamos with cycles and strong feedbacks, *Astrophys. J. Suppl.* **53**, 243–268 (1983).
3. G. A. Glatzmaier, Numerical simulations of stellar convective dynamos: II. Field propagation in the convection zone, *Astrophys. J.* **291**, 300–307 (1985).
4. M. Meneguzzi, U. Frisch and A. Pouquet, Helical and nonhelical turbulent dynamos, *Phys. Rev. Lett.* **47**, 1060–1064 (1981).
5. M. Meneguzzi and A. Pouquet, Turbulent dynamos driven by convection, *J. Fluid Mech.* **205**, 297–312 (1989).
6. S. Kida, S. Yanase and J. Mizushima, Statistical properties of MHD turbulence and turbulent dynamo, *Phys. Fluid. A*, **3**, 457–465 (1991).
7. A. Brandenburg, R. L. Jennings, Å. Nordlund, R. F. Stein and I. Tuominen, The role of overshoot in solar activity: A direct simulation of the dynamo, in *The Sun and Cool Stars: Activity, Magnetism, Dynamos*, edited by I. Tuominen, D. Moss and G. Rüdiger, pp. 86–88. Lecture Notes in Physics **380**. Springer, Berlin (1991).
8. Å. Nordlund, A. Brandenburg, R. L. Jennings, M. Rieutord, J. Ruokolainen, R. F. Stein and I. Tuominen, Dynamo action in stratified convection with overshoot, *Astrophys. J.* **392**, 647–652 (1992).
9. Ya. B. Zeldovich, A. A. Ruzmaikin, D. D. Sokoloff, *Magnetic Fields in Astrophysics*. Gordon and Breach, New York (1983).
10. E. D. Siggia, Numerical study of small-scale intermittency in three-dimensional turbulence, *J. Fluid Mech.* **107**, 375–406 (1981).
11. R. M. Kerr, Higher-order derivative correlations and the alignment of small-scale structures in isotropic numerical turbulence, *J. Fluid Mech.* **153**, 31–58 (1985).
12. A. Vincent and M. Meneguzzi, The spatial structure and statistical properties of homogeneous turbulence, *J. Fluid Mech.* **225**, 1–20 (1991).
13. A. Brandenburg, R. L. Jennings, Å. Nordlund, M. Rieutord, R. F. Stein and I. Tuominen, Magnetic structures in a dynamo simulation, *J. Fluid Mech.* submitted.
14. A. Brandenburg, I. Procaccia, D. Segel and A. Vincent, Fractal level sets and multifractal fields in direct simulations of turbulence, *Phys. Rev. A*, **46**, 4819–4828 (1992).
15. Wm. T. Ashurst, A. R. Kerstein, R. M. Kerr and C. H. Gibson, Alignment of vorticity and scalar gradient with strain rate in simulated Navier–Stokes turbulence, *Phys. Fluid.* **30**, 2343–2353 (1987).
16. R. M. Kerr, Histograms of helicity and strain in numerical turbulence, *Phys. Rev. Lett.* **59**, 783–786 (1987).
17. A. Vincent and M. Meneguzzi, On the dynamics of vortex tubes in homogeneous turbulence, *J. Fluid Mech.* **258**, 245–254 (1994).

18. P. Vieillefosse, Local interaction between vorticity and shear in a perfect incompressible fluid, *J. Physique* **43**, 837–842 (1982).
19. P. Vieillefosse, Internal motion of a small element of fluid in an inviscid flow, *Physica A* **125**, 150–162 (1984).
20. J. C. Neu, The dynamics of stretched vortices, *J. Fluid Mech.* **143**, 253–276 (1984).
21. J. Kurths and A. Brandenburg, Lyapunov exponents for hydromagnetic convection, *Phys. Rev. A* **44**, R3427–R3429 (1991).
22. A. Pouquet, U. Frisch and J. Léorat, Strong MHD helical turbulence and the nonlinear dynamo effect, *J. Fluid Mech.* **77**, 321–354 (1976).
23. A. M. Soward, Fast dynamos, in *Lectures on Solar and Planetary Dynamos*, edited by M. R. E. Proctor and A. D. Gilbert. pp. 181–217 Cambridge University Press, Cambridge (1994).
24. H. K. Moffatt, S. Kida and K. Ohkitani, Stretched vortices--the sinews of turbulence; large-Reynolds-number asymptotics, *J. Fluid Mech.* **259**, 241–264 (1994).
25. I. Klapper and M. Tabor, A Lagrangian study of 3D MHD dynamics and alignment in the neighbourhood of points with null or weak magnetic field, Preprint (1993).
26. B. B. Mandelbrot, Intermittent turbulence in self-similar cascades: divergence of high moments and dimension of the carrier, *J. Fluid Mech.* **62**, 331–358 (1974).
27. P. Constantin and I. Procaccia, Dimension of the carrier of turbulence: Intermittency in fluid mechanics, *Phys. Rev.* **46**, 4736–4741 (1992).
28. I. Procaccia, A. Brandenburg, M. H. Jensen and A. Vincent, The fractal dimension of iso-vorticity structures in 3-dimensional turbulence, *Europhys. Lett.* **19**, 183–187 (1992).
29. D. Biskamp, Geometric properties of level surfaces in MHD turbulence, *Europhys. Lett.* **21**, 563–567 (1993).
30. P. Grassberger and I. Procaccia, Characterisation of strange attractors, *Phys. Rev. Lett.* **50**, 346–349 (1983).
31. H. G. E. Hentschel and I. Procaccia, The infinite number of generalised dimensions of fractals and strange attractors, *Physica D* **8**, 435–444 (1983).
32. T. C. Halsey, M. H. Jensen, L. P. Kadanoff, I. Procaccia and B. I. Shraiman, Fractal measures and their singularities: The characterisation of strange sets, *Phys. Rev. A* **33**, 1141–1151 (1986).
33. Y. Du and E. Ott, Fractal dimensions of fast dynamo magnetic fields, *Physica D* **67**, 387–417 (1993).
34. C. Meneveau and K. R. Sreenivasan, The multifractal nature of turbulent energy dissipation, *J. Fluid Mech.* **224**, 429–484 (1991).
35. H. Hasimoto, A soliton in a vortex filament, *J. Fluid Mech.* **51**, 477–485 (1972).
36. E. J. Hopfinger, F. K. Browand and Y. Gagne, Turbulence and waves in a rotating tank, *J. Fluid Mech.* **125**, 505–534 (1982).
37. J. Villasenor and A. Vincent, An algorithm for space recognition and time tracking of vorticity tubes in turbulence, *CVGIP: Image Understanding* **55**, 27–35 (1992).
38. D. Biskamp, Scaling properties in MHD turbulence, *Chaos, Solitons & Fractals* **5**(10) 1779–1793 (1995).
39. A. Chhabra and R. V. Jensen, Direct determination of the $f(\alpha)$ singularity spectrum, *Phys. Rev. Lett.* **62**, 1327–1330 (1989).
40. J. K. Lawrence, A. A. Ruzmaikin and A. C. Cadavid, Multifractal measure of the solar magnetic field, *Astrophys. J.* **417**, 805–811 (1993).
41. E. Ott, Y. Du, K. R. Sreenivasan, A. Juneja and A. K. Suri, Sign-singular measures: fast magnetic dynamos, and high-Reynolds-number fluid turbulence, *Phys. Rev. Lett.* **69**, 2654–2657 (1992).
42. A. L. Bertozzi, A. B. Chhabra, L. P. Kadanoff, E. Ott and S. I. Vainshtein, On dynamo generation of magnetic flux and fractal properties of the field, Preprint (1993).
43. S. I. Vainshtein, Y. Du and K. R. Sreenivasan, Sign-singular measure and its association with turbulent scalings, *Phys. Rev. E* **49**, R2521–R2524 (1994).
44. M. Steenbeck, F. Krause and K.-H. Rädler, Berechnung der mittleren Lorentz-Feldstärke $\overline{\mathbf{v} \times \mathbf{B}}$ für ein elektrisch leitendendes Medium in turbulenter, durch Coriolis-Kräfte beeinflußter Bewegung, *Z. Naturforsch. A*, **21**, 369–376 (1966). See also the translation in Roberts and Stix, The turbulent dynamo . . ., Technical Note 60, NCAR, Boulder, Colorado (1971).
45. G. Rüdiger and A. Brandenburg, A solar dynamo in the overshoot layer: cycle period and butterfly diagram, *Astron. Astrophys* (in press).